Novel Imperfection Method for Post-Buckling Strength of C-Sectioned CFS Members

Ozge Gizem CAGRICI[1]
Rafet AKTEPE[2]
Burcu GULDUR ERKAL[3*]

ABSTRACT

The overall behavior of cold-formed steel (CFS) members is significantly affected from existing geometric imperfections. In this work, a mode shape-based imperfection coefficient computation method is developed to investigate the effects of initial geometric imperfections on member behavior. The point clouds of CFS members are collected and used to extract imperfection distributions and coefficients. The computed coefficients are integrated into the numerical model for analysis. Finally, axial loading tests are conducted to compare the numerical and experimental results. The results obtained using mode shape-based imperfection coefficients are generally closer to the experimental results than the common method used in practice.

Keywords: Cold-formed steel members, geometric imperfection detection, 3D scanning, finite element analysis, effects of initial geometric imperfections, automated deviation detection, column tests.

1. INTRODUCTION

The use of CFS is widespread in low-rise residential and industrial buildings. Especially in recent years, CFS usage has progressed visibly with advancing technology and increased research on this subject. From a usage point of view, CFS has many advantages. CFS has a high strength-to-weight ratio, dimensional stability, does not expand with humidity, etc. Even though CFS construction has several advantages, the members are prone to geometric imperfections during manufacturing, transportation, and installation. These geometric imperfections then significantly affect the individual behavior of CFS members.

Previous research performed on CFS structures showed that the accuracy of the numerical models generated to analyze the behavior of CFS members is directly dependent on the model inputs. In particular, how the geometric imperfections in the CFS members are reflected in the numerical model significantly changes the analysis results. This paper aims to use point clouds collected from CFS members by three-dimensional scanning technology to detect each CFS member's geometric imperfections automatically. The detected geometric imperfections are then represented in terms of mode shapes determined by an eigen-buckling analysis. Finally, the obtained mode shape-based imperfection coefficients are integrated into the numerical model to investigate the effects of geometric imperfection on CFS member behavior. The obtained numerical results are then compared with experimental results.

Several studies in the literature focused only on extracting geometric defects from CFS members. Peterman [1] used a specialized setup to measure imperfections at seven different spots (one specific location at a time) around the cross-section. Seven locations at the cross-sectional level were used by McAnallen, Padilla-Llano [2] to measure imperfection fields. They created a standard method for representing geometric imperfections using these observations as well as measurements from earlier studies. Zhao, Tootkaboni [3] created a test system that comprises a 2D line laser spanning widths up to 240 mm as the first attempt to apply 3D measurements for CFS geometric imperfection distribution extraction. To study the buckling deformation of built-up CFS columns, Salomon, Fratamico [4] used high-resolution optical cameras and computer vision techniques to construct 3D models that included position and time data. High-fidelity measurements of geometric imperfections were carried out by Zhao, Tootkaboni [5], who then used these data to characterize the distributions of geometric imperfections per different simulation techniques. In another investigation, cross-section dimensions and imperfections were determined using laser scan data of CFS members by Zhao, Tootkaboni [6]. Finally, to measure variations in CFS channel sections, Selvaraj and Madhavan [7] employed a 3D non-contact laser scanning technique. For the extraction of geometric imperfections, 27 deviation measurement points at the cross-section level were used. However, the effects of the extracted defects on CFS member behavior were not investigated in these studies.

The following studies, on the other hand, have concentrated both on extracting geometric defects and examining how they affect the behavior of CFS members. In Dubina and Ungureanu [8], several methods were developed to detect geometric imperfections and their integration into the finite element model. They discussed the effects of local and distortional geometric imperfections on buckling strength. Another study was performed to model geometric imperfections using different methods and compared the obtained results with the experimental results [9]. Zeinoddini and Schafer [10] developed a technique that combines modal approaches and spectral representations to extract the distributions of geometric imperfections. Nonlinear collapse analysis was performed using the obtained imperfection distributions. Garifullin and Nackenhorst [11] conducted a nonlinear buckling analysis on C-section columns. The sensitivity of the load-bearing capacity of CFS members to the geometric imperfections was examined. Another numerical study investigated the effect of initial geometric imperfections on the ultimate moment capacity of simply-supported sigma-sectioned CFS beams [12]. Sadovský, Kriváček [13] examined the effects of initial geometric imperfections on CFS members' buckling strength by performing computational modeling. This study aimed to determine the most unfavorable geometric imperfections represented by the eigenmode shapes in the geometric and material-nonlinear finite element analysis (FEA)

of CFS members with imperfections (GMNIA). Zeinoddini and Schafer [14] performed an experimental study to characterize global bow, camber, and twist in CFS- lipped channel members and record the dimensional changes. Martins, Dinis [15] carried out a numerical investigation to observe the influence of local–distortional (L–D) interaction on the ultimate strength of web-stiffened and lipped channel CFS columns. In Li [16], the effects of geometric imperfections on the buckling mode interaction of C-sectioned CFS members were observed. Nonlinear collapse analyses were performed using ABAQUS/CAE [17] to investigate these interactions. Deformations obtained from the analyses were divided into local, distortional, and global deformation modes.

The previous studies mentioned above, although valuable, have limitations in representing the actual geometry of CFS members due to the use of a limited number of data points. To overcome this limitation, it is crucial to develop robust strategies that can extract defects from entire geometric representations. In this paper, an improvement is made by obtaining the geometric imperfections of each CFS member from point clouds captured through a 3D data collection system. These extracted imperfections are then integrated into numerical models to investigate their effects on member behavior. Additionally, axial loading tests are conducted on the previously scanned CFS members to validate the results obtained from the numerical models. Prior research on axial loading tests of CFS members and numerical modeling is also examined to ensure successful tests and the development of efficient numerical models capable of accurately capturing observed behavior [18-22].

The structure of the work presented in this paper is as follows. To begin with, the point clouds that fully reflect the geometries of the scanned objects are obtained. Later, the method developed to obtain geometric imperfections in the members using point clouds automatically is laid out. Then, the obtained geometric imperfections are integrated into the numerical models to investigate the effects of these imperfections on the members' behavior. The finite element analysis performed to observe these effects is carried out in two steps. First, an eigenvalue elastic buckling analysis is performed to establish the buckling modes (eigenmodes). The members' extracted geometric imperfections are then decomposed into the deflected member shapes corresponding to each buckling mode to obtain imperfection coefficients. Second, a general geometrical and material nonlinear static analysis with imperfections (GMNIA) was performed to simulate the structural behavior of CFS members. Parallel to these studies, axial compression tests are carried out on previously scanned members. The experimental results are then compared with the finite element analysis outputs obtained for traditional and point cloud-based geometric imperfection integration strategies.

2. POINT CLOUD DATA COLLECTION

In this work, geometric imperfections on CFS members are extracted automatically from point clouds collected via a 3D data collection system.

2.1. Details of the Available CFS Members

In total, 16 C-sectioned CFS members with varying dimensions and with/without pre-punched slotted web holes are examined in this work. The investigated CFS members are labeled as follows: cross-section type – nominal web height – member length – specimen

with or without holes – sequence number. All the investigated CFS members have a flange width of 45 mm, web height of 90 mm, lip width of 10 mm, and thickness of 1.2 mm. For example, C-90-900-NH-1 represents a first C-sectioned member with a web height of 90 mm, member length of 900 mm, and no holes.

2.2. Scanner used for Point Cloud Collection

A 3D optical scanning system, a Breuckmann 3D scanner (rebranded as SmartScan, HEXAGON [24]) with the highest accuracy of 3 microns, is used to collect point clouds. This scanner offers mono and color scanning with medium to super-high resolutions. The field of view varies from 30 mm to 1.5 meters. Each CFS member is positioned 1 meter away from the scanner during scanning, and the high-resolution option is selected. The scanner is then moved around the member to obtain full coverage. Further detail on the collected point clouds for each investigated CFS member can be found in Guldur Erkal and Cagrici [25].

3. AUTOMATED GEOMETRIC IMPERFECTION DETECTION AND QUANTIFICATION METHOD

The geometric imperfection extraction in this work is performed using the method laid out in Guldur Erkal and Cagrici [25]. This method focuses on conducting an automated cross-section-based geometric imperfection detection and quantification. As a result, representative keypoints at successive cross-sections along the longitudinal axis of the CFS members are extracted and used for geometric imperfection quantification. The geometric imperfections are computed based on common representations given in Figure 1. The automated cross-section-based geometric imperfection detection and quantification results for the investigated CFS members are presented in Guldur Erkal and Cagrici [25].

4. MODE SHAPE-BASED GEOMETRIC IMPERFECTION COEFFICIENT EXTRACTION

The effects of the extracted geometric imperfections on member behavior could be examined by introducing these imperfections into numerical models. Even though there are several ways to perform this (such as mesh alteration or constant imperfection coefficient usage), they either increase the computational cost or underestimate the member strength. Thus, this paper introduces a novel mode shape-based geometric imperfection coefficient computation. This method represents each member's existing geometric imperfections in buckling mode shapes.

In this section, the details of the performed eigen-buckling analysis are given. The appropriate least-squares method specializing in overdetermined equations, which is used to reconstruct the geometric imperfections based on the mode shapes obtained by the performed eigen-buckling analysis, is then laid out.

The mode shapes that form the geometric imperfections can be determined by eigen-buckling analysis. The geometric imperfection representations are obtained by combining the relevant local, distortional, or overall buckling modes of the cross-section or member. They are later used to invoke geometric nonlinearity during further numerical analysis [26]. Thus, the
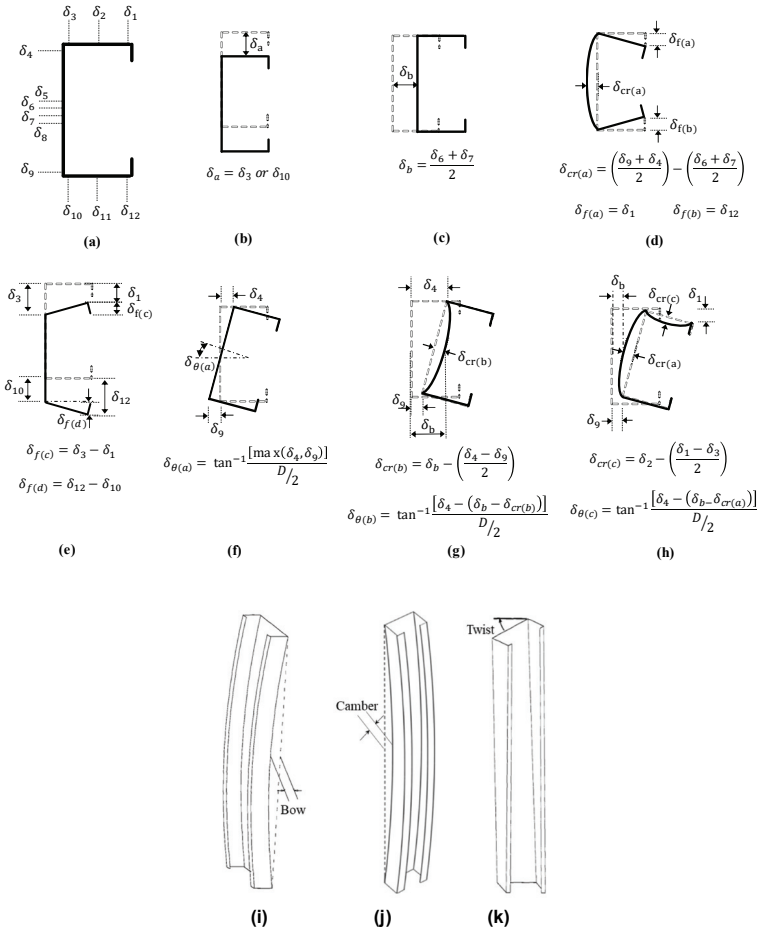
Figure 1 - Local geometric imperfection formulations: (a) keypoint deviations, (b) cross-section shift orthogonal to the flanges, (c) cross-section shift orthogonal to the web, (d) convex crown, (e) flare, (f) twist only, (g) twist with concave crown, and (h) twist with convex crown and concave flange; and global imperfection representations: (i) bow, (j) camber, and (k) twist (revisited from Guldur Erkal and Cagrici [25]).

standard application for taking the imperfection effects into account during numerical analysis is to perform an eigen-buckling analysis and to introduce the imperfections to the numerical model by multiplying the buckling mode shape outputs with specific coefficients. Generally, the first mode is multiplied by 0.1t, t is the thickness of the CFS member, and the consecutive mode shapes are multiplied with decreasing coefficients, i.e., 0.1t for mode shape 1, 0.05t for mode shape 2, and the rest of the coefficients decrease with the same trend. Koiter [27] states imperfection sensitivity may be most efficiently expressed as a function of imperfection magnitudes in the buckling mode shapes. Thus, the maximum imperfections provide a reasonable lower bound strength analysis criterion.

4.1. Eigen-Buckling Analysis

In this study, ABAQUS/CAE [17] is used for both eigen-buckling and GMNIA to simulate the behavior of the C-sectioned CFS columns under axial loading. For eigen-buckling analysis, subspace iteration is chosen as the eigenvalue extraction method. The roundness of corners is not considered in the ABAQUS models. Consequently, residual stresses and cold-work effects are neglected [13, 28-30].

4.1.1. Element Type and Mesh

All C-sectioned CFS columns are modeled by selecting the S4R thin shell element. A convergence study was carried out to determine the suitable mesh size, considering both axial load capacity predictions and computational time. Based on the results of the convergence study, the appropriate mesh size for the elements was determined as 2.5 mm x 2.5 mm (Figure 2).
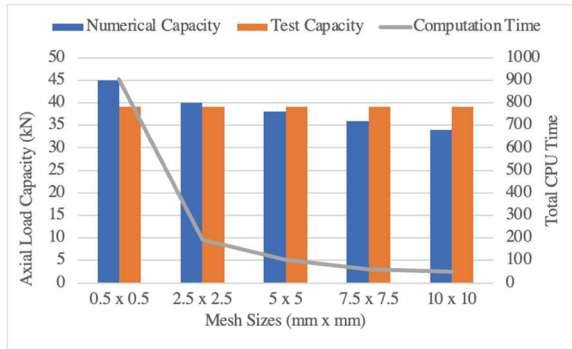

Figure 2 - Comparison of the test capacity with numerical capacities and computational times.

4.1.2. Material Properties

The material properties of the specimens are determined by tensile coupon tests according to the ASTM E8/E8M Standard ASTM-E8/E8M [31]. Three tensile coupons were sampled from the specimens. The obtained engineering stress-strain curves of the tensile coupon tests are given in Figure 3.
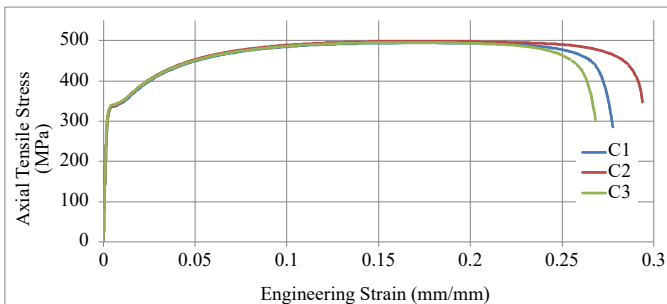

Figure 3 - Engineering stress-strain curves of the test coupons C1, C2, and C3.

The engineering stress (σ_{eng})-engineering strain (ε_{eng}) data obtained from tensile coupon tests need to be converted into true stress (σ_{true})-true strain (ε_{true}) data before being inserted into the numerical models. Equations [1] and [2] are used for the initial conversion. Finally, the obtained true strain is converted into plastic strain ($\varepsilon_{true\ (pl)}$) data with Equation [3] to model material nonlinearity with von Mises yield criterion and isotropic hardening.

$$\sigma_{true} = \sigma_{eng}(1 + \varepsilon_{eng}) \tag{1}$$

$$\varepsilon_{true} = \ln\left(1 + \varepsilon_{eng}\right) \tag{2}$$

$$\varepsilon_{true\ (pl)} = \ln\left(1 + \varepsilon_{eng}\right) - \frac{\sigma_{true}}{E} \tag{3}$$

4.1.3. Material Modelling

Material nonlinearity of the specimens is modeled with von Mises yield criteria and isotropic hardening. Yield strength of 333 MPa, an ultimate strength of 496 MPa, and a Young's Modulus of 186 MPa, obtained from tensile coupon tests, are used.

4.1.4. Boundary Conditions

All columns are modeled using fixed support conditions. Reference nodes at the centroid of cross-sections are defined at each end. All the nodes at one end of the column located on the surface are tied to the reference node using the 'rigid-body' 'fixed' constraint. All degrees of freedom are restricted at one reference node (bottom end). In contrast, all degrees of freedom are restricted at the opposite end except in the longitudinal direction, where the loading is applied.

4.1.5. Mode Shapes

The first 20 mode shapes of each investigated CFS member are extracted for performing mode shape-based imperfection coefficient extraction. Sample mode shape results for C-90-1100-NH-1 obtained after eigen-buckling analysis is given in Figure 4.
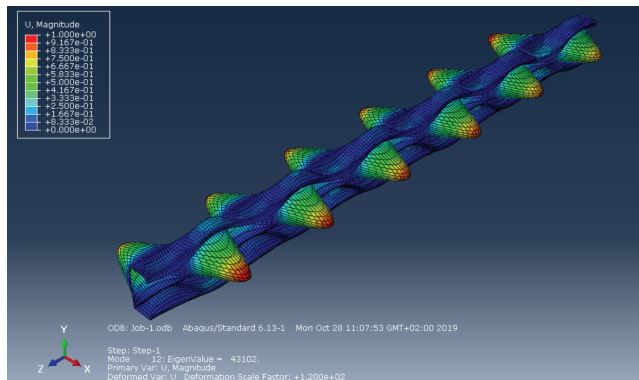

Figure 4 - C-sectioned column, C-90-1100-NH-1 - Mode shape 12

4.2. Overdetermined Equations

The magnitudes of geometric imperfections are already determined using the previously described automated geometric imperfection detection and quantification method. To perform the imperfection quantification, keypoints located at each cross-section cut along the length of each member are extracted (Figure 5a). The finite element mesh is specifically tailored to match the extracted keypoint locations. The same positive and negative directions used for automated geometric imperfection detection and quantification method are used to record mode shape displacements. If the movement is outside the reference cross-section, the displacements are recorded as positive. The displacements are recorded as negative values if the movement is inward. Figure 5b shows both positive displacement directions for different subgroups of 12 keypoints with respect to the reference cross-section of a point cloud sample. Figure 5c shows the matching keypoints (with the point cloud cross-sections) on the ABAQUS model of C-90-1100-NH-1.

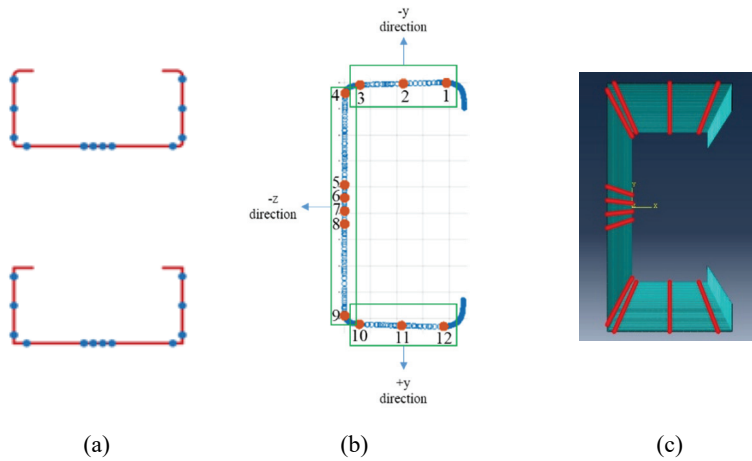(a)   (b)   (c)

Figure 5 - (a) Accurate and simplified cross-section representation with keypoints, (b) positive displacement directions for different subgroups of 12 keypoints with respect to the reference cross-section (with keypoint labels), and (b) keypoints on the ABAQUS model of C-90-1100-NH-1.

Once the displacements corresponding to each keypoint for all 20 mode shapes are recorded, the entire set of equations is solved to get the best overall coefficient that takes 12 keypoints at each cross-section cut into account to capture the geometric imperfection on CFS members. Sample geometric imperfection representation for a single keypoint is given in Figure 6(a). It should be noted that the extracted geometric imperfections at each keypoint are later shifted towards the horizontal axis to get a mean value of zero. This step is essential since the mean values of all the displacement recorded for local mode shapes are zero. Thus, if the mode shapes will be used for coefficient determination, the geometric imperfection should be suitable for decomposed representation. Figure 6(a) shows a sample displacement variation of the 12th keypoint along the length of C-90-1100-NH-1. Displacement variations of the 12th keypoint along the length of C-90-1100-NH-1 for the first 20 mode shapes are shown in Figure 6(b).

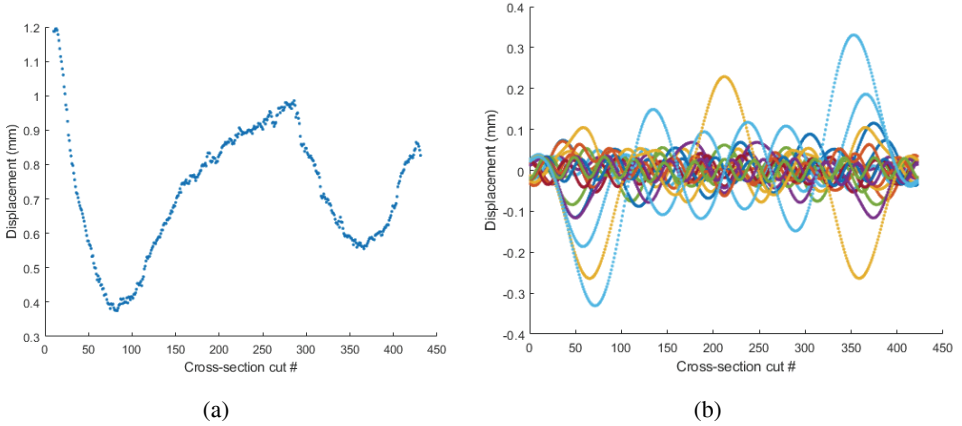(a)   (b)

Figure 6 - Displacement variations of the 12th keypoint along the length of C-90-1100-NH-1 obtained (a) from the member's point cloud and (a) from the analysis model for the first 20 mode shapes.

Consider a system of linear equations (Equation [4]):

$$y = Hx \qquad (4)$$

If the total number of equations is greater than the unknowns (**H** is a tall matrix), then the system is specified as overdetermined. An overdetermined system almost never has a solution. For this research, the sizes of the **H** are 4332x20, 4812x20, 5292x20, and 5772x20. There are 361, 401, 441, and 481 strips for 900 mm, 1000 mm, 1100 mm, and 1200 mm long CFS members, respectively. At each cross-section, there are 12 keypoints; thus, the row size is equal to the cross-section cut number (361, 401, 441, 481) times 12. The rows represent back-to-back cross-section cuts for each keypoint, whereas the columns correspond to the displacements extracted for the first 20 mode shapes corresponding to each keypoint. The common least squares solution that can be adapted for this type of problem is given in Equation [5]):

$$\min_{x}\|y - Hx\|_2^2 \xrightarrow{yields} x = (H^TH)^{-1}H^Ty \qquad (5)$$

For this study, global imperfections are favored, meaning that the weights of the keypoints primarily associated with global imperfections (keypoints located on the web) are increased. For these cases, it is required to minimize the weighted square error, i.e., $\sum_n w_n r_n^2$ where r is the residual, or error, $r = y - Hx$, and w_n are positive weights. This corresponds to minimizing $\left\|W^{1/2}(y - Hx)\right\|_2^2$ where W is the diagonal matrix, $[W]_{n,n} = w_n$. Using Equation [5] leads to Equation [6]:

$$\min_{x}\left\|W^{1/2}(y - Hx)\right\|_2^2 \xrightarrow{yields} x = (H^TWH)^{-1}H^TWy \qquad (6)$$

37

Figure 7 presents sample MSB coefficient extraction results for the imperfection distribution shown in Figure 6(a). The mode shapes shown in Figure 6(b) are used for this extraction.
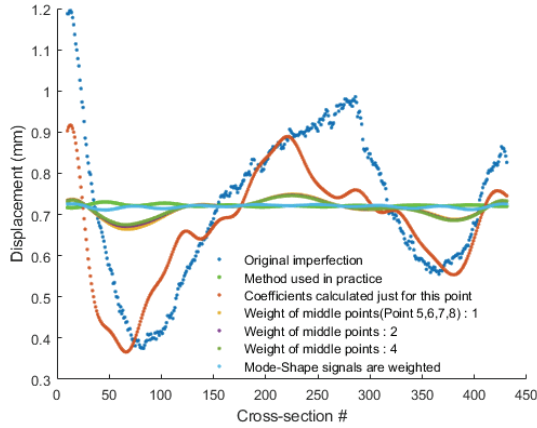

Figure 7 - Sample result for MSB coefficient extraction for C-90-1100-NH-1: Original imperfection, 0.1t multiplication, result with coefficients calculated just for the investigated point, and different weighted coefficient results are displayed.

4.3. Finite Element Analysis

GMNIA is then performed to investigate the effects of MSB geometric imperfection coefficients on member behavior. The determined MSB coefficients are introduced to the model by multiplying these coefficients with corresponding mode shapes obtained from the eigen-buckling analysis, comparable to the approach adopted for the traditional method of geometric imperfection modeling. For this study, the arc-length method (Riks) is chosen for GMNIA. After an eigenvalue buckling analysis, GMNIA is often performed to provide complete information about a structure's collapse [32]. Figure 8 shows the final deformed shape of C-90-1100-NH-1 as a result of GMNIA.
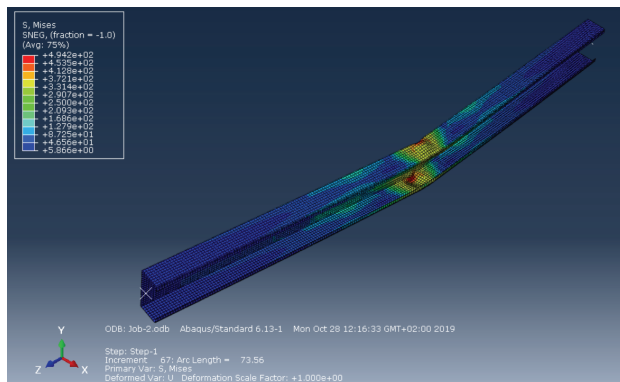

Figure 8 - Final deformed shape result of the GMNIA performed on C-90-1100-NH-1.

5. AXIAL LOADING TESTS OF CFS MEMBERS

Axial loading tests are then performed on the 3D-scanned C-sectioned CFS members. In this section, the utilized test setup and the testing procedure are presented.

5.1. Test Setup

A test setup is specifically designed and built for axial loading of cold-formed steel members. This test device comprises bottom and top steel frames connected by four steel bars, each 50 mm in diameter. The upper frame is formed by connecting two 1950 mm long IPE330 profiles using IPE330 profiles at three locations, at two ends and in the middle. The lower frame is constructed by connecting two 3000 mm long IPE330 profiles at 5 locations. The connections are performed at the ends, in the middle, and close to the locations where the 50 mm diameter bars pass. As the upper frame is mobile, CFS columns with varying lengths were tested (900 – 1200 mm). Further detail on the test setup and related schematics could be found in Guldur Erkal and Cagrici [25].

5.2. Testing Procedure

The described testing frame is capable of applying uniaxial loads up to 30 tons. A hydraulic cylinder (Enerpac RR7513) is attached to the upper frame for axial column tests. Beneath the hydraulic cylinder, a load cell (Esit HSC-V) with a 60-ton capacity is mounted.

The column test setup is equipped with a series of Kyowa DTH 10 mm, 30 mm, and 50 mm linear variable displacement transducers (LVDT) to record the displacements of the specimen throughout the experiments. However, only the average results obtained from three LVDTs (one 10 mm and two 30 mm) attached to the top plate are utilized. During the tests, both the eccentricity between the centerline of the specimens and the load axis, as well as the lateral stability, were actively monitored and effectively addressed.

All 16 CFS members are individually tested. As a sample, the pre- and post-test images of C-90-1000-NH-2 are presented in Figure 9a-b. There are three LVDTs attached to the top plate (loading plate). The top plate LVDT results vs. load cell readings are plotted for C-90-1000-NH-2 in Figure 9c.
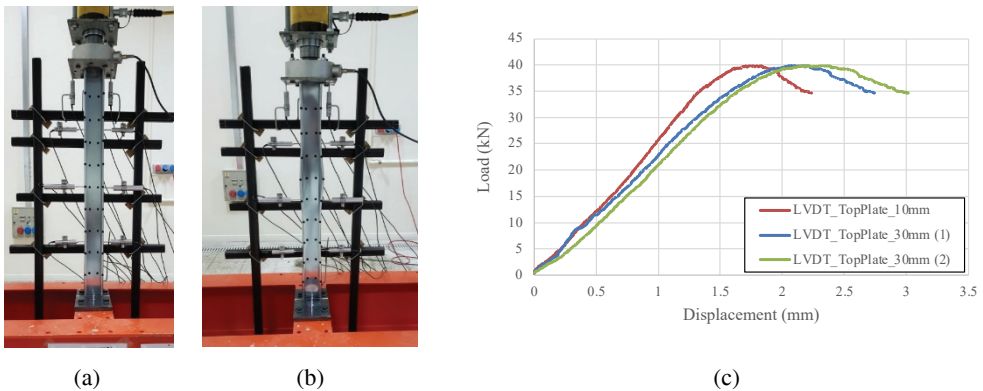

(a)   (b)   (c)

Figure 9 - Images taken before (a) and (b) after the axial loading test for C-90-1000-NH-2 and the top plate LVDT recordings vs. load plot.

6. RESULTS AND DISCUSSIONS

This section focuses on the results and discussions related to the previous sections. First, to verify the suitability of the collected point clouds for automated geometric imperfection detection and quantification, the point cloud resolutions are displayed. Hand measurements are used to validate the accuracy of the gathered point clouds' dimensions.

The mode shape-based imperfection coefficients of one CFS member are then given. The changes in the imperfection representations caused by different geometric imperfection coefficients are discussed. Finally, the effects of the determined coefficients on CFS member behavior are discussed.

In this study, a desktop suite with an Intel(R) Xeon CPU E5-1650 v3 @ 3.50GHz processor, 48GB RAM, 64-bit operating system, and NVIDIA Quadro K22 graphics card is used to generate the algorithms, run the developed algorithms, and conduct finite element analysis. Finite element analyses are completed by using ABAQUS. All the algorithm development and testing are carried out in MatLab [33] release 2019a. The processing times display variability depending on the length of the member. The average processing time for an individual CFS member, including pre-processing and geometric imperfection extraction, is 300 seconds. Mode-shape-based coefficient extraction is completed in 15 seconds for all 16 C-sectioned CFS members. Last, finite element analysis, including eigen-buckling and GMNIA, takes 15 minutes for each CFS member.

6.1. Point Cloud Resolution

Previous studies have revealed that point cloud precision depends on factors such as point cloud density, registration precision, and angle of incidence [34-37]. A detailed resolution study is performed on all investigated CFS members' point clouds by examining the density of each point cloud. The results showed that the gathered point clouds' resolutions change between 0.018 and 0.033 mm. The average resolution for all members is 0.025 mm. Thus, the collected point clouds are expected to detect geometric imperfections larger than the average resolution value.

In Guldur Erkal and Cagrici [25], the minimum values for local, distortional, and global imperfections collected from previous studies and the related standards computed for 900 – 1200 mm are presented. The obtained resolution values are then compared with the reported minimum values of geometric imperfections in the literature. This comparison demonstrates that the point cloud resolutions are sufficient for geometric imperfection detection and quantification. The captured resolutions are much smaller than the published minimum imperfection values.

6.2. Point Cloud Validation

The measured dimensions of the investigated CFS members are then compared with the dimensions detected by performing point cloud processing. In Guldur Erkal and Cagrici [25], both micrometer-measured and automatically detected dimensions of the CFS members are reported. The comparison between the measured and detected dimensions is also performed to compute the errors.

For both web and flanges of all 16 CFS members, the computed error values are under 2%. The mean error is 1.15% and 1.63% for the web and flanges, respectively, whereas the standard deviations are 0.49% and 0.38% for the web and flanges. The conducted validation investigation confirmed that the gathered point clouds accurately depict the as-is geometry of the actual condition of the investigated CFS members.

6.3. Mode Shape-based Geometric Imperfection Coefficient Extraction Results

In Section 4, the details of the developed mode shape-based geometric imperfection coefficient extraction are presented. Table 1 shows the mode shape-based geometric imperfection coefficients for C-90-900-H-2 given as an example for the first 20 modes. The second column of the table shows the coefficients for which all the keypoints have the same importance and weight in overdetermined equations. The third column shows the coefficients computed where the keypoints on the web, five, six, seven, and eight, receive a weight of two (Figure 5). A weight of four is used for the web keypoints to calculate the coefficients in the fourth column. The coefficients in the fifth column are computed as follows: the coefficients in the first column (no weight case) are multiplied with decreasing values such as 1.0, 0.5, 0.25, and this goes on until the 20th mode.

Table 1 - Mode shape-based geometric imperfection coefficients for C-90-900-H-2 are given for the first 20 modes.

Mode Shape #	No Weight	Middle Points Weight =2	Middle Points Weight =4	Weighted
1	-0.308	-0.299	-0.292	-0.308
2	-0.049	-0.052	-0.052	-0.025
3	0.122	0.152	0.176	0.031
4	0.030	0.024	0.017	0.004
5	0.051	0.045	0.040	0.003
6	-0.049	-0.044	-0.039	-0.002
7	-0.046	-0.039	-0.032	-0.001
8	0.168	0.186	0.201	0.001
9	-0.077	-0.075	-0.071	0.000
10	0.041	0.010	-0.016	0.000
11	0.027	0.045	0.058	0.000
12	0.026	0.029	0.030	0.000
13	0.068	0.063	0.055	0.000
14	-0.060	-0.047	-0.042	0.000
15	-0.080	-0.068	-0.059	0.000
16	-0.085	-0.129	-0.164	0.000
17	0.479	0.490	0.505	0.000
18	-0.016	-0.015	-0.014	0.000
19	0.346	0.390	0.425	0.000
20	0.059	0.045	0.031	0.000

The reconstructed geometric imperfections for 12 keypoints of C-90-900-H-2 with varying MSB coefficients are given in Figure 10. The original imperfections are obtained from the point clouds by performing automated geometric imperfection extraction, plotted with blue dots in each figure. The imperfections reconstructed using the 0.1t multiplication method are labeled 'Method used in practice.' Red dots give the coefficients specifically computed for the investigated keypoint (Case 1). Thus, they represent the closest result to the original imperfection distribution for a selected keypoint. The rest of the plots are reconstructed using the coefficients that account for the entire set of 12 keypoints. These plots represent the cases: no weight (or the weight for each keypoint is one) (Case 2), the weights of middle keypoints (5-8, located on the web) equal to 2 (Case 3), the weights of middle keypoints (5-8, situated on the web) equal to 4 (Case 4), and finally, the coefficients for the mode shapes are multiplied with decreasing values (Case 5) as mentioned before. The keypoint labels are shown in Figure 5.
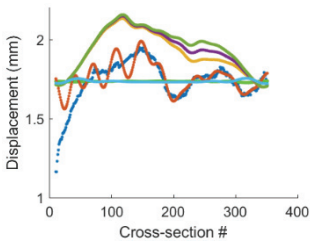
As seen in Figure 10, the reconstructed imperfection plots obtained by using the method in practice fail to represent the original imperfection in all keypoints. This trend can be observed for the other investigated CFS members as well. Therefore, the GMNIA results obtained using the traditional method generally cannot be considered to represent the actual results for the as-is geometric imperfections on a CFS member. The method in practice is presented with bright green dots in Figure 10.

It should be noted that the reconstruction works better for the point located on the flanges (1-2 and 11-12). However, as the keypoints get closer to the web, the reconstructions fail even for the investigated keypoint (Case 1), i.e., Figure 10e-h. Regardless of the keypoint location, the worst results are obtained either by the method in practice or in Case 5. These two approaches almost always fail to represent the original imperfection distribution. Cases 2, 3, and 4 generally result in similar reconstructions. It could be concluded that changing the weights of web keypoints does not significantly affect the final reconstructed representation, especially in the absence of mode shapes representing global buckling modes. It should be noted that the accuracy of the generated mode shape-based imperfection coefficient extraction method improves with an increasing number of varying mode shape representations. Therefore, other mode shapes could be included in the analysis to enhance generated signal quality and coefficient extraction, or the effect of global buckling modes should be forced into the coefficient extraction process.
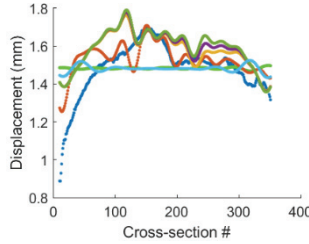
Table 2 lists the squared error values for the method in practice and Cases 1-5, along with the total signal energy computed for each CFS member. The total signal energy is computed by summing the squares of the geometric imperfection distributions extracted from the point clouds. It can be seen from the table that the closest result to the original imperfection is always obtained with Case 1, as the computed squared error values are always the lowest. However, Case 1 only represents one location on the cross-section. It does not represent the entire set of 12 keypoints. Thus, Case 1 is not considered in GMNIA. The second-best results are obtained for Case 2, for which the entire collection of keypoints is considered. Case 2-4 give worse results than Case 1, and Case 5 is very similar to the method in practice. Thus, in the GMNIA, only the method in practice and Case 2 are investigated and compared.

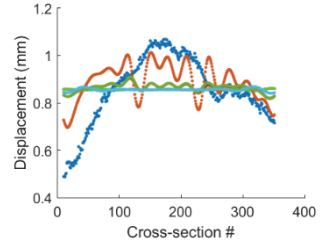*Table 2 - Squared error values for method in practice and Cases 1-5.*

Specimen	Total Signal Energy	Total Squared Error for Method in Practice	Total Squared Error for Single Point Coef. (Case 1)	Total Squared Error for No Weight (Case 2)	Total Squared Error for Middle Points Weight=2 (Case 3)	Total Squared Error for Middle Points Weight=4 (Case 4)	Total Squared Error for Weighted Coefficients (Case 5)
C-90-900-NH-1	636.40	644.74	549.27	595.83	596.07	596.45	627.15
C-90-900-NH-2	610.23	616.40	527.67	570.05	570.12	570.25	603.84
C-90-900-H-1	774.80	785.24	494.73	680.38	687.58	705.88	754.10
C-90-900-H-2	665.76	676.64	393.32	496.93	498.32	501.64	644.03
C-90-1000-NH-1	1148.17	1155.66	971.42	1081.25	1081.30	1081.36	1130.26
C-90-1000-NH-2	1886.18	1894.71	1671.82	1792.13	1792.32	1792.59	1860.56
C-90-1000-H-1	1133.45	1140.10	844.53	1079.20	1080.57	1083.65	1114.76
C-90-1000-H-2	1716.80	1725.09	1210.94	1638.93	1641.11	1646.18	1690.58
C-90-1100-NH-1	715.35	724.14	643.15	693.95	694.14	694.39	710.71
C-90-1100-NH-2	655.77	662.91	589.16	640.48	640.58	640.71	653.18
C-90-1100-H-1	627.18	632.22	412.38	581.04	583.60	589.44	622.80
C-90-1100-H-2	572.91	576.18	343.78	526.87	531.75	543.07	571.19
C-90-1200-H-1	487.71	492.32	342.25	465.37	467.68	472.75	484.75
C-90-1200-H-2	654.28	659.10	464.95	628.18	630.58	635.84	650.91
C-90-1200-NH-1	828.01	834.85	746.27	819.70	819.81	819.97	825.92
C-90-1200-NH-2	824.58	832.63	755.89	812.54	812.63	812.75	821.26

(a)

(b)

(c)

(d)

(e)

(f)

Legend for the figures:

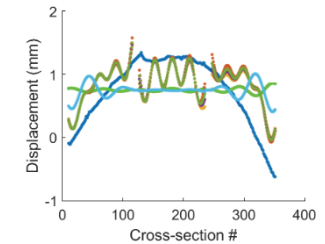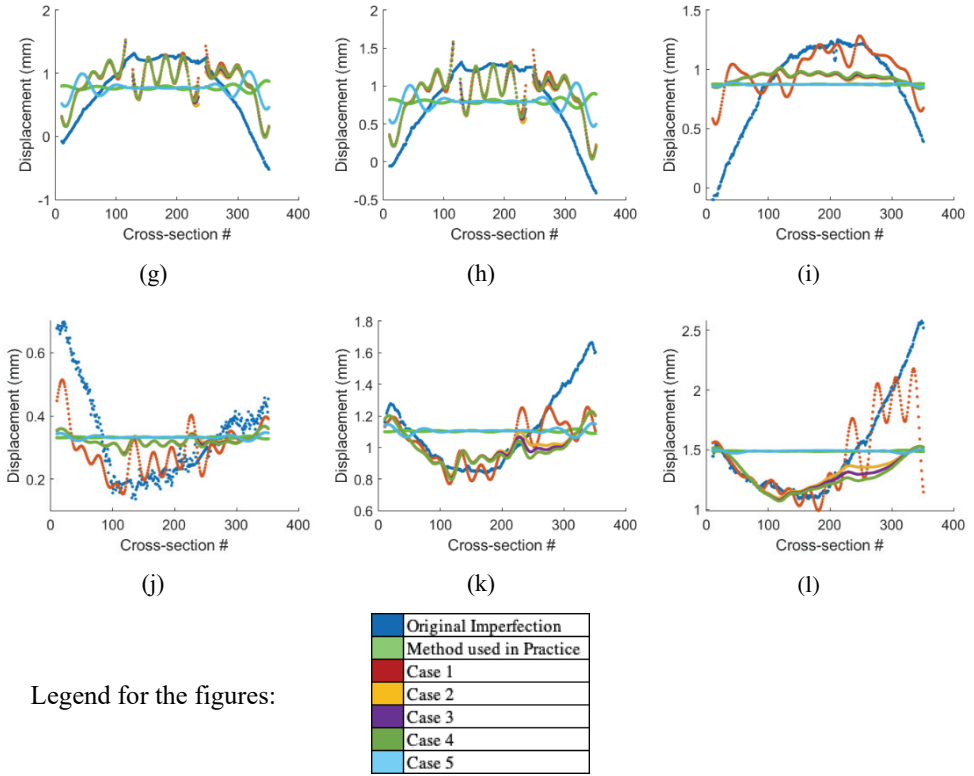| Original Imperfection |
| Method used in Practice |
| Case 1 |
| Case 2 |
| Case 3 |
| Case 4 |
| Case 5 |
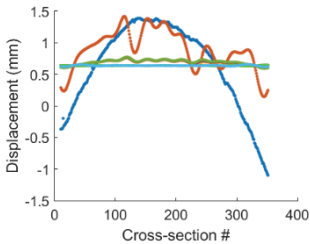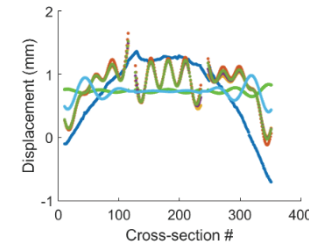
Figure 10 - Reconstructed geometric imperfections for 12 keypoints of C-90-900-H-2 with varying MSB coefficients.

6.3.1. Results of GMNIA with Varying MSB Coefficients

This section displays the GMNIA results for all the investigated CFS members. Analyses are terminated when the displacement capacities obtained during the experiment are obtained. The top displacement vs. load curves obtained from nonlinear analysis for mode shape-based geometric imperfection coefficients, 0.1t coefficient, and collected test data are given in Figure 11 for all investigated CFS members. The test data for comparing the numerical results are obtained by averaging the data from the three LVDTs attached to the top plate.
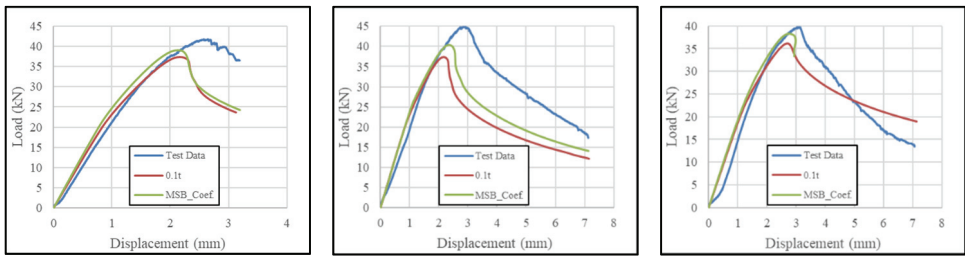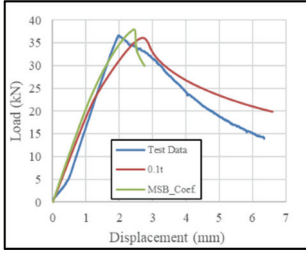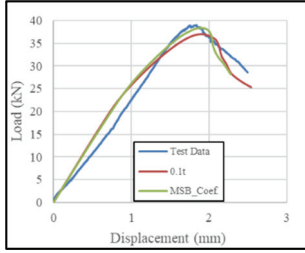

(a) C-90-900-NH-1   (b) C-90-900-NH-2   (c) C-90-900-H-1
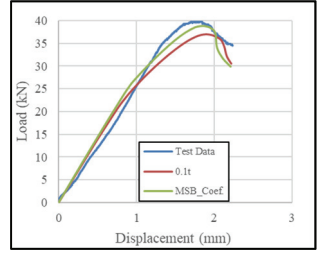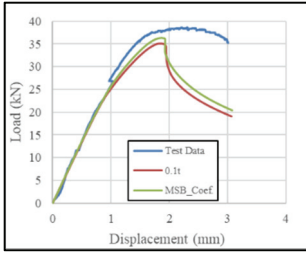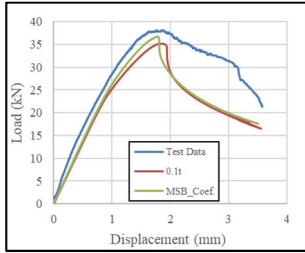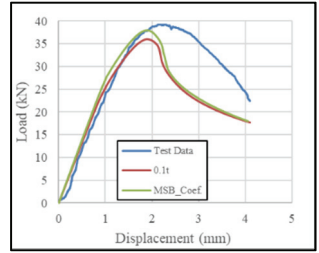
(d) C-90-900-H-2
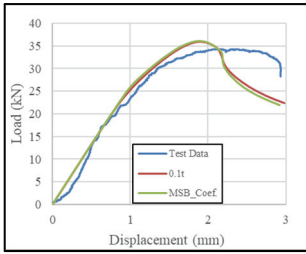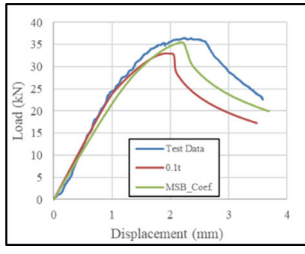
(e) C-90-1000-NH-1

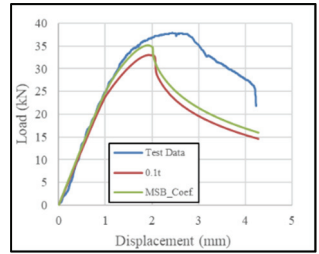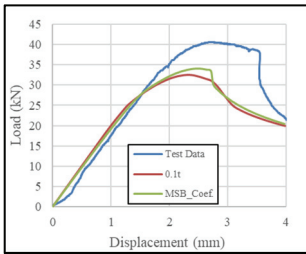(f) C-90-1000-NH-2

(g) C-90-1000-H-1
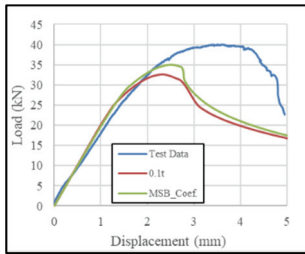
(h) C-90-1000-H-2

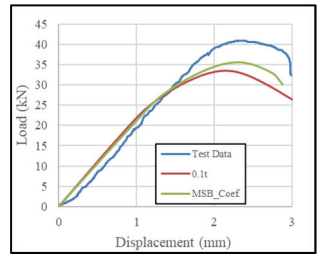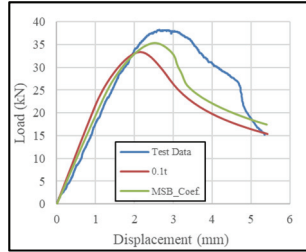(i) C-90-1100-NH-1

(j) C-90-1100-NH-2

(k) C-90-1100-H-1

(l) C-90-1100-H-2

(m) C-90-1200-H-1

(n) C-90-1200-H-2

(o) C-90-1200-NH-1

(p) C-90-1200-NH-1

Figure 11 - Top displacement vs. load curves obtained for all investigated CFS members for various cases.

The GMNIA results showed that the method in practice generally underestimates the capacity of the investigated CFS members. The GMNIAs performed with the imperfection distributions obtained by reconstruction mode shapes provide closer results to CFS members' actual behavior. However, the results obtained with the MSB coefficients also underestimate the member capacity, and at the same time, this method sometimes underestimates the displacement capacities.

Table 3 presents the initial slope and energy results obtained from GMNIAs for 0.1t and MSB coefficients and experiment results. The errors are computed by comparing the MSB coefficient results with the experiment results. The errors calculated for the initial slopes are mostly less than 10%, which indicates that the GMNIA results are in good accordance with the experiments. However, the average error for the energy, which represents the area under the top displacement vs. load curves, is approximately 18%. The lowest computed value is 1.45%, and the highest value of nearly 57%. Even though the total displacement capacity obtained from the GMNIAs matches the experiment results, in most of the GMNIAs, there is a significant capacity loss after the ultimate load capacity is reached. Therefore, the energy values computed for the GMNIA results for the same total displacement capacity as experiments are always lower than the values obtained for experiment results.

AISI-S100 is later used to calculate yielding, flexural buckling, torsional buckling, flexural torsional buckling, local buckling, and distortional buckling capacities. The test results are then compared with the GMNIA results, and the design capacities are computed with AISI-S100. The ultimate load capacities computed for local buckling are critical for all CFS members. Table 4 reports the ultimate load capacity of the investigated members recorded in experiments, computed with AISI-S100 (local buckling), obtained from GMNIA with 0.1t coefficient and GMNIA with MSB coefficients. The experiment results are higher than the axial load capacities computed via AISI-S100. It is observed that the results obtained from GMNIA with a 0.1t coefficient are on the safe side. The GMNIA results with a 0.1t coefficient give lower ultimate load capacities than the experiment results but closer to the axial load capacities computed via AISI-S100. Finally, the GMNIA results with MSB coefficients are higher than the axial load capacities calculated via AISI-S100 but more comparable to the experiment results.

7. CONCLUSIONS

In this work, a numerical and experimental study was conducted to examine the impact of geometric imperfections on the behavior of cold-formed steel (CFS) members. Point clouds representing the real geometry of 16 CFS members were collected using a 3D optical scanner. The results showed that these point clouds effectively represented the geometric imperfections in the members. These imperfections varied significantly across different members, indicating that a constant value for local imperfections would not accurately represent individual member conditions.

Geometric imperfections were integrated into finite element models using MSB coefficients to perform GMNIA. Mode shapes obtained from eigen-buckling analysis were used to reconstruct imperfection distributions in the finite element model. However, it was found that reconstructing the actual deformed shape of a CFS member using mode shapes was not possible. If only a single keypoint on each cross-section was considered, reconstructed imperfection distributions could be used.

To validate the GMNIA results, axial loading tests were conducted on the investigated CFS members. The buckling load, axial and lateral displacements, and material properties were monitored and recorded during the tests. The experimental results were used to validate the numerical models.

The GMNIA results using varying geometric imperfection coefficients showed that the method in practice was over-conservative. Models generated with MSB coefficients provided slightly better representation of member behavior but were still conservative. The study concluded that improving the representation of geometric imperfections or boundary conditions could enhance the accuracy of finite element model results.

It should be noted that while the method in practice is conservative and easy to implement, it is important to evaluate alternative approaches for optimal design and utilization of CFS frames, especially in seismic regions. Addressing overdesign and accurately simulating geometric imperfections is crucial. The development of an easy-to-use methodology for extracting imperfections and advancements in high-resolution 3D scanning offer opportunities to enhance the proposed method for more accurate results in the future. This will improve overall performance assessment and maximize the benefits of CFS structures in construction.

In future studies, it is recommended to focus on keypoint coefficients for individual keypoints as they provide the best representation of imperfection distribution. Additionally, exploring the integration of global modes into the coefficient extraction process could be valuable. However, assigning suitable weights to global modes poses a challenge as they are forcibly extracted. Further research is needed to address these aspects and enhance the analysis accuracy.

Acknowledgments

Table 3 - Initial slope and energy results for GMNIA results for 0.1t and MSB coefficients and experiment results and the associated errors.

Specimen	Initial Slope (kN/mm)			Initial Slope	Energy (kN.mm)			Energy
	Exp.	0.1t Coef.	MSB Coef.	Error (%)	Exp.	0.1t Coef.	MSB Coef.	Error (%)
C-90-900-NH-1	21.35	20.58	22.70	6.32	87.89	76.58	82.13	-6.55
C-90-900-NH-2	20.08	20.58	21.32	6.18	199.46	144.44	160.93	-19.32
C-90-900-H-1	17.30	16.49	17.60	1.74	165.12	168.81	71.08	-56.95
C-90-900-H-2	19.03	16.49	19.09	0.27	139.60	158.18	65.06	-53.40
C-90-1000-NH-1	22.24	24.49	25.15	13.10	60.36	62.92	56.30	-6.73
C-90-1000-NH-2	25.11	24.49	26.64	6.10	56.65	54.11	55.82	-1.45
C-90-1000-H-1	28.00	25.52	25.85	-7.69	86.34	68.94	71.97	-16.64
C-90-1000-H-2	27.04	25.52	26.47	-2.08	100.36	74.37	79.10	-21.19
C-90-1100-NH-1	24.97	24.04	26.08	4.45	114.82	94.45	97.85	-14.78
C-90-1100-NH-2	25.21	25.65	26.13	3.62	73.66	72.45	70.85	-3.82
C-90-1100-H-1	25.73	23.49	21.51	-16.39	92.65	74.86	84.35	-8.96
C-90-1100-H-2	26.53	23.49	24.87	-6.25	119.48	87.50	93.50	-21.75
C-90-1200-H-1	18.77	19.03	18.95	0.95	107.47	90.10	90.96	-15.37
C-90-1200-H-2	17.04	19.03	19.15	12.39	144.83	108.89	113.62	-21.55
C-90-1200-NH-1	20.47	21.08	21.05	2.86	77.76	71.03	69.98	-10.00
C-90-1200-NH-2	17.32	21.46	19.17	10.71	138.68	118.02	124.81	-10.00

Table 4 - Axial load capacities of the investigated members recorded in experiments, computed with AISI-S100, obtained from GMNIA with 0.1t imperfection, and GMNIA with MSB coefficients.

Specimen	Experimental		AISI Design Strength		GMNIA + Method in Practice (0.1t)		GMNIA + Reconstruction with MSB Coef.	
	P_{Exp} (kN)	Failure mode	P_{AISI} (kN)	Fail. mode	P_{MiP} (kN)	Failure mode	P_{MSBC} (kN)	Failure mode
C-90-900-NH-1	41.78	Local + Distortional Buck.	38.98	Local Buck.	37.35	Local Buck.	39.06	Local Buck.
C-90-900-NH-2	45.05	Local Buck.	38.98	Local Buck.	37.35	Local Buck.	40.37	Local Buck.
C-90-900-H-1	39.79	Local Buckling at Hole	38.98	Local Buck.	36.10	Local Buckling at Hole	38.27	Local Buckling at Hole
C-90-900-H-2	36.66	Local Buckling at Hole	38.98	Local Buck.	36.10	Local Buckling at Hole	37.80	Local Buckling at Hole
C-90-1000-NH-1	38.94	Local + Distortional Buck.	36.77	Local Buck.	36.98	Local Buck.	38.32	Local Buck.
C-90-1000-NH-2	39.79	Local + Distortional Buck.	36.77	Local Buck.	36.98	Local Buck.	38.84	Local Buck.
C-90-1000-H-1	38.65	Local Buck.	36.77	Local Buck.	35.11	Local Buckling at Hole	36.33	Local Buckling at Hole
C-90-1000-H-2	38.08	Local + Distortional Buck.	36.77	Local Buck.	35.11	Local Buckling at Hole	36.61	Local Buckling at Hole
C-90-1100-NH-1	39.22	Local Buck.	34.46	Local Buck.	36.01	Local Buck.	37.90	Local Buck.
C-90-1100-NH-2	34.25	Local Buck.	34.46	Local Buck.	36.01	Local Buck.	36.11	Local Buck.
C-90-1100-H-1	36.52	Local Buckling at Hole	34.46	Local Buck.	33.08	Local Buckling at Hole	35.38	Local Buckling at Hole
C-90-1100-H-2	37.94	Local Buckling at Hole	34.46	Local Buck.	33.08	Local Buckling at Hole	35.17	Local Buckling at Hole
C-90-1200-H-1	40.64	Local Buckling at Hole	32.11	Local Buck.	32.56	Local Buckling at Hole	34.05	Local Buckling at Hole
C-90-1200-H-2	40.07	Local Buckling at Hole	32.11	Local Buck.	32.56	Local Buckling at Hole	34.97	Local Buckling at Hole
C-90-1200-NH-1	40.92	Local Buck.	32.11	Local Buck.	33.45	Local Buck.	35.59	Local Buck.
C-90-1200-NH-2	38.22	Local Buck.	32.11	Local Buck.	33.45	Local Buck.	35.37	Local Buck.

References

[1] Peterman KD. Experiments on the stability of sheathed cold-formed steel studs under axial load and bending. Baltimore, MD, USA: John's Hopkins University; 2012.

[2] McAnallen L, Padilla-Llano D, Zhao X, Moen C, Schafer B, Eatherton M. Initial geometric imperfection measurement and characterization of cold-formed steel C-section structural members with 3D non-contact measurement techniques. Proceedings of the Structural Stability Research Council. Toronto, Canada2014.

[3] Zhao X, Tootkaboni M, Schafer B. Development of a laser-based geometric imperfection measurement platform with application to cold-formed steel construction. Experimental Mechanics. 2015;55:1779-90.

[4] Salomon AL, Fratamico D, Schafer BW, Moen CD. Full field cold-formed steel column buckling measurements with high resolution image-based reconstruction. Proceedings of the Annual Stability Conference Structural Stability Research Council. Orlando, FL, USA2016.

[5] Zhao X, Tootkaboni MP, Schafer BW. High fidelity imperfection measurements and characterization for cold-formed steel members. Proceedings of the 7th International Conference on Coupled Instabilities in Metal Structures. Baltimore, MD, USA2016.

[6] Zhao X, Tootkaboni M, Schafer BW. Laser-based cross-section measurement of cold-formed steel members: model reconstruction and application. Thin-Walled Structures. 2017;120:70-80.

[7] Selvaraj S, Madhavan M. Geometric imperfection measurements and validations on cold-formed steel channels using 3D noncontact laser scanner. Journal of Structural Engineering. 2018;144.

[8] Dubina D, Ungureanu V. Effect of imperfections on numerical simulation of instability behaviour of cold-formed steel members. Thin-Walled Structures. 2002;40:239-62.

[9] Bonada J, Casafont M, Roure F, Pastor M. Selection of the Initial Geometrical Imperfection in Nonlinear FE Analysis of Cold-formed Steel Rack Columns. Thin-walled Structures. 2012;51:99-111.

[10] Zeinoddini V, Schafer B. Simulation of geometric imperfections in cold-formed steel members using spectral representation approach. Thin-Walled Structures. 2012;60:105-17.

[11] Garifullin M, Nackenhorst U. Computational Analysis of Cold-formed Steel Columns with Initial Imperfections. Procedia Engineering. 2015;117:1073-9.

[12] Gendy BL, Hanna M. Effect of Geometric Imperfections on the Ultimate Moment Capacity of Cold-Formed Sigma-Shape Sections. HBRC Journal. 2017;13:163-70.

[13] Sadovský Z, Kriváček J, Ivančo V, Ďuricová A. Computational modelling of geometric imperfections and buckling strength of cold-formed steel. Journal of Constructional Steel Research. 2012;78:1-7.

[14] Zeinoddini V, Schafer BW. Global imperfections and dimensional variations in cold-formed steel members. International Journal of Structural Stability and Dynamics. 2011;11:829-54.

[15] Martins AD, Dinis PB, Camotim D. On the Influence of Local-Distortional Interaction in the Behaviour and Design of Cold-Formed Steel Web-Stiffened Lipped Channel Columns. Thin-Walled Structures. 2016;101:181-204.

[16] Li Z. Stochastically simulated mode interactions of thin-walled cold-formed steel members using modal identification. Thin-Walled Structures. 2018;128:171-83.

[17] ABAQUS/CAE. ABAQUS Users' Guide 2019. Dassault Systemes: Paris, France: Dassault Systemes; 2019.

[18] Ye J, Hajirasouliha I, Becque J. Experimental investigation of local-flexural interactive buckling of cold-formed steel channel columns. Thin-walled structures. 2018;125:245-58.

[19] dos Santos ES, Batista EM, Camotim D. Experimental investigation concerning lipped channel columns undergoing local–distortional–global buckling mode interaction. Thin-Walled Structures. 2012;54:19-34.

[20] Dinis PB, Camotim D, Silvestre N. FEM-based analysis of the local-plate/distortional mode interaction in cold-formed steel lipped channel columns. Computers & Structures. 2007;85:1461-74.

[21] Camotim D, Dinis PB. Coupled instabilities with distortional buckling in cold-formed steel lipped channel columns. Thin-Walled Structures. 2011;49:562-75.

[22] Chou S, Chai G, Ling L. Finite element technique for design of stub columns. Thin-walled structures. 2000;37:97-112.

[23] Moen CD, Schafer B. Elastic buckling of thin plates with holes in compression or bending. Thin-Walled Structures. 2009;47:1597-607.

[24] HEXAGON. SmartScan. 2022.

[25] Guldur Erkal B, Cagrici OG. Automated Geometric Imperfection Detection and Quantification of CFS Members from Point Clouds. KSCE Journal of Civil Engineering. 2022.

[26] Eurocode 3 - Part 1-3. Eurocode 3: Design of Steel Structures, Part 1-3 - Design of Cold-Formed Steel Structures: ECCS Eurocode Design Manuals; 2012.

[27] Koiter WT. On the stability of elastic equilibrium: National Aeronautics and Space Administration; 1967.

[28] Schafer BW, Li Z, Moen CD. Computational modeling of cold-formed steel. Thin-Walled Structures. 2010;48:752-62.

[29] Schafer B, Peköz T. Computational modeling of cold-formed steel: Characterizing geometric imperfections and residual stresses. Journal of Constructional Steel Research. 1998;47:193-210.

[30] Gendy BL, Hanna MT. Effect of geometric imperfections on the ultimate moment capacity of cold-formed sigma-shape sections. HBRC Journal. 2019;13:163-70.

[31] ASTM-E8/E8M. Standard Test Methods for Tension Testing of Metallic Materials. West Conshohocken, PA.: ASTM International; 2013.

[32] Simulia D. ABAQUS 6.11 analysis user's manual. Abaqus. 2011;6:22.2.

[33] MatLab. MATLAB and Statistics Toolbox Release 2019a. Natick, MA, USA: The MathWorks, Inc.; 2019.

[34] Kashani AG, Olsen MJ, Parrish CE, Wilson N. A review of LiDAR radiometric processing: From ad hoc intensity correction to rigorous radiometric calibration. Sensors. 2015;15:28099-128.

[35] Laefer DF, Gannon J, Deely E. Reliability of crack detection methods for baseline condition assessments. Journal of Infrastructure Systems. 2010;16:129-37.

[36] Laefer DF, Truong-Hong L, Carr H, Singh M. Crack detection limits in unit based masonry with terrestrial laser scanning. Ndt & E International. 2014;62:66-76.

[37] Olsen MJ, Kuester F, Chang BJ, Hutchinson TC. Terrestrial laser scanning-based structural damage assessment. Journal of Computing in Civil Engineering. 2010;24:264-72.